

Analytical thermal model of conduction mode double sided arc welding

Y. Kwon and D. C. Weckman*

An analytical thermal model of conduction mode double sided arc welding (DSAW) has been derived and used to predict the weld pool dimensions and shapes and temperatures within 2.5 and 1.15 mm thick AA5182 Al alloy sheets as functions of the primary DSAW parameters. Separate Gaussian distributed arc heat sources from a plasma arc welding and gas tungsten arc welding torch were assumed to act on the top and bottom surfaces of the sheets. There was excellent correlation between observed and predicted DSAW weld pool dimensions and shapes provided that suitable values for arc efficiencies and distribution coefficients for the two separate arcs were used in the model. The model is capable of predicting weld pool dimensions and shapes of both full and partial penetration conduction mode DSAW welds made in Al alloy sheet, the welding speed at which there is a transition from full to partial penetration welding and the speed above which no melting occurs.

Keywords: Analytical thermal model, Double sided arc welding, Al sheet

Introduction

Automotive manufacturers are coming under increasing regulatory pressure to improve the overall fleet mileage of their automobiles. Consequently, there is much interest in development and assessment of advanced materials and manufacturing technologies that will allow fabrication of lighter automotive bodies and structural components. For example, CO₂ laser welding of tailor welded blanks (TWBs) of conventional automotive steel sheets is a well established manufacturing technology that has been shown to provide up to 30% weight savings for structural components.¹ Tailor welded blanks are composite blanks made from combinations of different sheet steel and galvanised coating thicknesses that are joined together along butt joints using full penetration square welds. Once welded, the TWB is stamped and formed into a structural component.

Further savings in automotive body weight can be realised by making TWBs from lighter Al alloys such as AA5182; however, the high thermal conductivity and thermal expansion coefficient, low absorptivity and tenacious Al oxide make the welding of wrought Al alloys more challenging than the welding of traditional sheet steel alloys.² To facilitate manufacturing of Al alloy TWBs in a high speed automotive production environment, new welding techniques must be identified and assessed. Thus, there have been numerous studies performed to examine the weldability of Al alloy sheets and TWBs using welding processes such as the electron

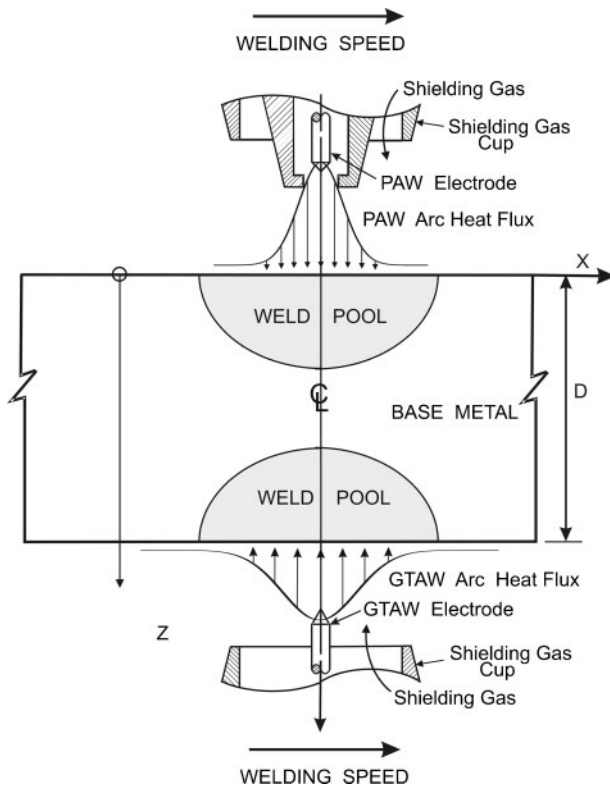
beam welding, Nd:YAG laser beam welding and variable polarity plasma arc welding (VPPAW) processes.^{3–11} However, weld defects such as undercutting, poor underbead quality and oxide removal, occluded gas porosity, hydrogen porosity and reduced weld metal strength due to loss of Mg in the weld metal have been shown to be problematic when using many of these processes.^{5–9}

The recently patented double sided arc welding (DSAW) process¹² is a relatively new arc welding process that uses one power supply and two torches. As shown in the schematic diagram of the DSAW process in Fig. 1, a plasma arc welding (PAW) torch is frequently used on one side of the plate and a PAW or gas tungsten arc welding (GTAW) torch is used on the other side of the plate. The arc is struck between the two torches and the weld specimens are then moved between the two torches at the welding speed thereby creating two separate arcs acting on the top and bottom surface of the specimens simultaneously. The plates to be welded are grounded and not part of the electric welding circuit. To date, the DSAW process has been used by Zhang *et al.*^{12–18} to produce vertical-up, keyhole mode welds in 6 to 12 mm thick plain carbon steel, stainless steel or Al alloy plates.

In a recent study, the feasibility of using the conduction mode DSAW process for high speed welding of 1.2 mm thick AA5182 Al alloy sheet for TWB applications was examined.^{19,20} This process, as illustrated in Fig. 1, was shown to have a number of advantages over laser beam welding and VPPAW for Al TWB applications. It provides cathodic etching of the Al oxide on both sides of the sheet rather than just on the top side. When used in the conduction mode as shown in Fig. 1, the weld bead quality on both sides of the sheet

Department of Mechanical and Mechatronics Engineering, University of Waterloo, Waterloo, Ontario N2L 3G1, Canada

*Corresponding author, email dweckman@uwaterloo.ca



1 Schematic diagram of DSAW process

was as good as single sided VPPAW conduction mode welds.^{10,11} In addition, the weld bead profile of the full and partial penetration DSAW welds was symmetrical through the sheet thickness.

If the DSAW process was used in the keyhole mode with the arc passing from the PAW electrode, straight through the keyhole in the sheet to the GTAW electrode, then two-dimensional (2D), analytical models such as Rosenthal's^{21,22} or Swift-Hook and Gick's²³ models of full penetration keyhole mode laser beam welding might be used to model the process. There have also been a number of attempts recently to develop more sophisticated numerical thermofluids models of this keyhole mode DSAW process.²⁴⁻²⁶ However, no models have as yet been derived for the conduction mode DSAW process.^{19,20}

Hong *et al.*²⁷ have shown that the effects of fluid flow on weld pool dimensions and shape in fusion welds are negligible for high thermal conductivity metals such as Al and Cu alloys. Thus, analytical thermal models of this conduction dominated problem can be expected to provide quite reasonable predictions of the weld pool shape and isotherms in the solid of the AA 5182 Al sheet used in the present study. Rosenthal's^{21,22} and Carslaw and Jaeger's²⁸ three-dimensional (3D) point heat source analytical models of conduction mode fusion welding have been widely used to predict the size of weld pools and cooling rates in plates of infinite thickness and finite thickness plates. However, Smartt *et al.*,²⁹ Tsai and Eagar³⁰ and Lu and Kou,³¹ have shown that the arc heat flux distributions of PAW and GTAW arcs are generally well described by a Gaussian distribution as shown schematically in Fig. 1. Also, the distribution coefficient or effective width of the heat source has been shown to depend on the arc gap, electrode geometry, shielding gas composition and total welding power. Thus, Cline and

Anthony³² have since used Green's function to derive a solution for the temperature in a semi-infinite solid subjected to a moving Gaussian distributed heat source. This solution was later derived also by Eagar and Tsai³³ using the principle of superposition and used to show that correlation between predicted and observed GTAW weld pool shapes was much better when using a Gaussian distributed heat source model rather than a point heat source model.

In most welding applications, the plate is neither infinitely thick (3D solution) nor very thin (2D solution), but has a finite thickness. Rosenthal^{21,22} and Grong³⁴ showed that an analytical heat transfer model of welding of plates of finite thickness D , could be formulated using the infinite thickness plate solution and the 'method of images'. More recently, Manca *et al.*³⁵ derived directly an analytical solution for temperatures in a solid of finite thickness D , and finite width W , subject to a moving Gaussian distributed heat source.

The objective of the present study was to derive an analytical thermal model of the conduction mode DSAW process and to use this model to predict the weld pool dimensions and shape, and temperatures in thin sheets of AA 5182 Al as a function of the various DSAW process parameters. Such a model would facilitate better understanding of the effects of the weld process parameters on DSAW weld dimensions and shapes as well as provide a useful tool for weld procedure development. It could be used, for example, to predict the maximum possible welding speed, i.e. the welding speed at which there is a transition from full penetration to partial penetration as well as the speed above which no melting occurs for different combinations of sheet thickness, alloy composition, welding power, etc.

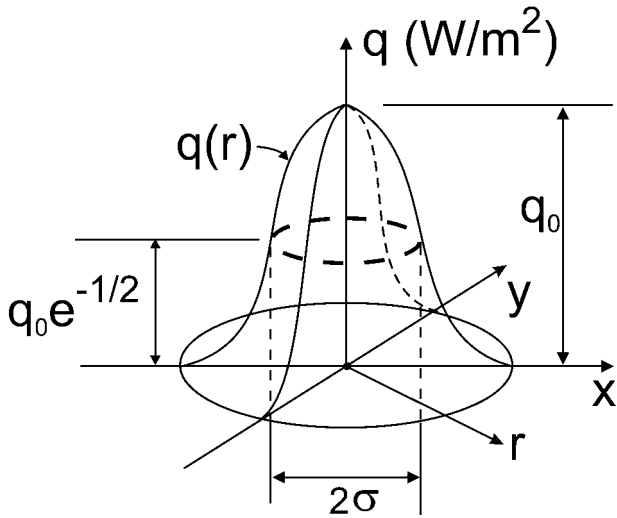
Mathematical problem

A schematic diagram of the DSAW process, the coordinate system and boundary conditions used in this study are shown in Fig. 1. As indicated, a 3D xyz Cartesian coordinate system in conjunction with a Euclidean coordinate framework was used to model the welding process. The y direction is out of the page.

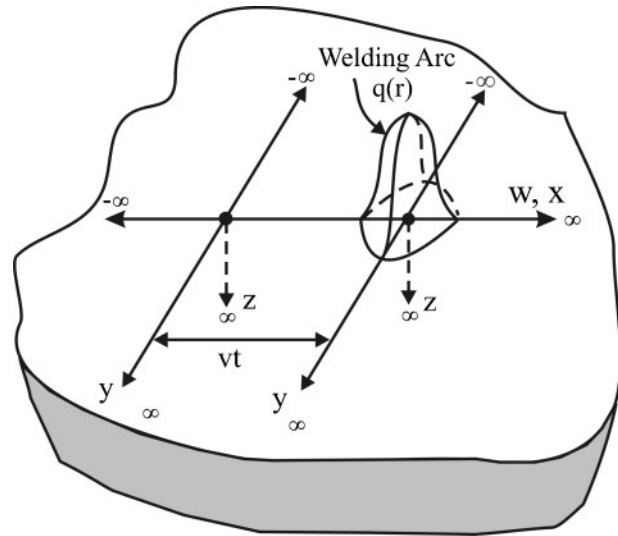
The DSAW process uses two arc welding torches. In this study, a PAW torch was used on the top of the sheet and a GTAW torch on the bottom of the sheet (see Fig. 1). The sheet was of thickness D , and was assumed to be infinitely large in the x and y directions. The initial temperature of the sheet T_0 , was assumed to be room temperature (295 K). Steady state conduction mode welding was assumed, where the arc heat input from the PAW and GTAW torches caused localised heating and melting of the base metal, thus forming the weld pools on the top and bottom surfaces of the sheet. Following the experimental measurements of Smartt *et al.*,²⁹ Tsai and Eagar³⁰ and Lu and Kou,³¹ the arc heat flux distributions of the PAW and GTAW arcs acting on the top and bottom surfaces of the plate were assumed to be well described by a Gaussian distribution as shown schematically in Fig. 2. The equation for this distribution is

$$q(r) = q_0 \exp\left[-\frac{r^2}{2\sigma^2}\right] = \frac{Q_w}{2\pi\sigma^2} \exp\left[-\frac{r^2}{2\sigma^2}\right] \quad (1)$$

where $q(r)$ is the heat flux (W m^{-2}), q_0 is the peak heat



2 Gaussian distributed arc heat flux $q(r)$, where the distribution parameter σ is the standard deviation of the Gaussian function and q_0 is the peak heat flux at $r=0$



3 Gaussian distributed arc heat flux source moving over the surface of a semi-infinite plate at welding speed v

flux ($W\ m^{-2}$) at $r=0$ where r is the radial position given by $r=(x^2+y^2)^{1/2}$, σ is the distribution coefficient for the Gaussian distribution (m), and Q_w is the net power input (W) given by $Q_w=\eta EI$ where η is the arc efficiency, E is the voltage and I is the current. As indicated in equation (1) and Fig. 2, σ is defined here as the radial position at which the heat flux $q(r)$, has decreased to $1/e^{1/2}$ ($\approx 60\%$) of the peak heat flux q_0 . Note that values of η and σ of the PAW and GTAW arcs were assumed to be different.

Following the assumptions originally made by Rosenthal,^{21,22} it was assumed that heat losses from the plate by convection or radiation were negligible, that the latent heat of fusion and fluid flow effects could be ignored, and that all thermophysical properties were constant. Table 1 shows the constant thermophysical material properties for AA5182 Al that were used including the solidus temperature T_s , the specific heat C_p , thermal conductivity k_t and density ρ .³⁶

Governing equation and initial and boundary conditions

Under the assumed conditions described in the previous section, the governing heat conduction equation in the solid plate using the Euclidean coordinate framework is^{22,37}

$$\frac{\partial^2 T}{\partial x^2} + \frac{\partial^2 T}{\partial y^2} + \frac{\partial^2 T}{\partial z^2} = \frac{1}{\alpha} \frac{\partial T}{\partial t} \tag{2}$$

where $\alpha=k_t/\rho C_p$ is thermal diffusivity ($m^2\ s^{-1}$), T is temperature (K) and t is time (s). A solution for this partial differential equation exists provided α is assumed to be constant.²² Following Rosenthal,²² solution of equation (2) must satisfy the following initial and

boundary conditions

$$T - T_0 = 0 \text{ for } t=0 \text{ and } r > 0 \tag{3}$$

$$T - T_0 = 0 \text{ for } 0 < t < \infty \text{ and } r \rightarrow \infty \tag{4}$$

where $r = (x^2 + y^2 + z^2)^{1/2}$. Finally, Gaussian distributed heat sources as described by equation (1) were assumed to move over the top and bottom surfaces of the solid in the x direction at the welding speed v .

Solution of governing equation and boundary conditions

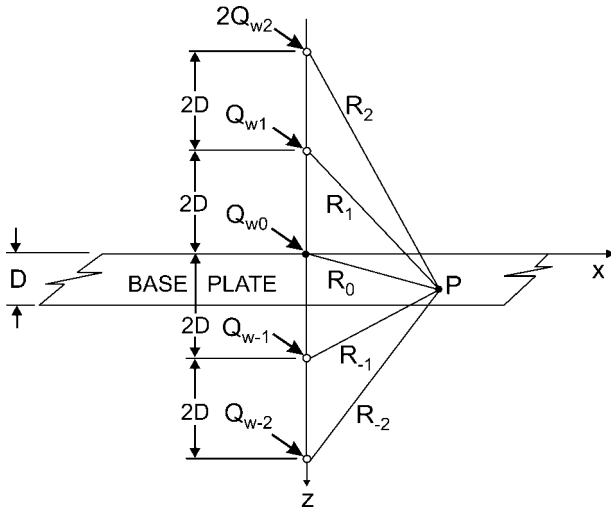
An analytical solution for the problem described above will be formulated using a combination of an existing solution for a very similar geometry, the ‘method of images’ and the ‘principle of superposition’. The authors begin here by considering a previously derived solution for a Gaussian distributed heat source moving over the surface of a semi-infinite solid in the x direction at a welding speed v , as shown in Fig. 3. In this case, the w, y, z coordinate system is fixed to the semi-infinite plate and a second coordinate system x, y, z is defined that moves with the Gaussian distributed heat source at the welding speed v . At any time t , the arc has moved a distance along the plate equal to vt . For large times, the temperatures within the plate relative to the heat source become quasi-steady state. Rosenthal^{21,22} has shown that for the case of a point heat source (i.e. $\sigma=0$), the temperature in the semi-infinite plate is given by

$$T - T_0 = \frac{Q_w}{2\pi k_t r} \exp\left[\frac{-v(x+r)}{2\alpha}\right] \tag{5}$$

Cline and Anthony³² and Eagar and Tsai³³ have since derived a solution for the temperature in the semi-infinite solid subjected to a moving Gaussian distributed heat source using two different approaches. In both cases, however, the solution for the temperature in the semi-infinite solid with a moving Gaussian distributed heat source was given by

Table 1 Constant thermophysical material properties of AA5182-O that were used for simulations³⁶

T_s , K	k_t , $W\ m^{-1}\ K^{-1}$	C_p , $J\ kg^{-1}\ K^{-1}$	ρ , $Mg\ m^{-3}$
850	123	904	2.65



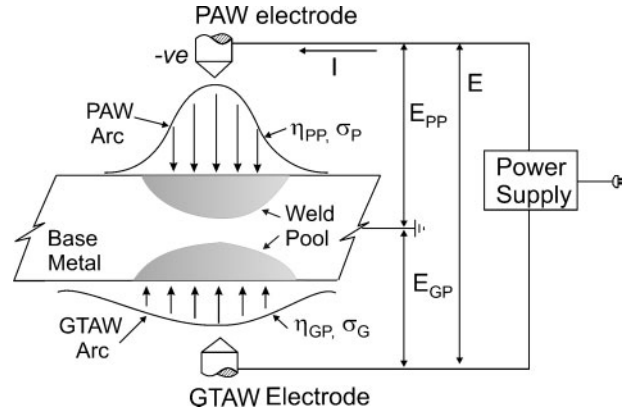
4 ‘Method of images’ using real and imaginary point sources ... Q_{w-1} , Q_{w0} , Q_{w1} , Q_{w2} , etc. acting on a plate of finite thickness D

$$T - T_0 = \frac{Q_w}{\pi \rho C_p} \int_0^\infty \frac{1}{(4\pi \alpha t)^{1/2} (2\alpha t + \sigma^2)} \exp \left\{ \frac{-[(x+vt)^2 + y^2]}{(4\alpha t + 2\sigma^2)} - \frac{z^2}{4\alpha t} \right\} dt \quad (6)$$

Cline and Anthony³² and Eagar and Tsai³³ have shown that equation (6) reduces to Rosenthal’s^{21,22} thick plate solution for welding with a point source (i.e. equation (5) above) when σ is allowed to go to zero and t to go to a very long time, i.e. $t \rightarrow \infty$.

Equation (6) provides the temperature in an infinite half space with a Gaussian distributed heat source moving over its surface in the x direction at a welding speed v . It is not valid, however, for plates with a finite thickness, such as the plate used in the present study of the DSAW process. Therefore, a general finite thickness plate model similar to that introduced by Rosenthal²² is required. Assuming that both plate surfaces are adiabatic and that the plate is of finite thickness D , then following Rosenthal²² and Grong,³⁴ the ‘method of images’ can be used to maintain the net flux of heat through both the top and bottom surface boundaries equal to zero. Thus, it is necessary to account for mirror reflections of the heat source with respect to the planes $z=0$ and $z=D$. Let $\{\dots Q_{w-2}, Q_{w-1}, Q_{w0}, Q_{w1}, Q_{w2}, \dots\}$ denote the sequence of imaginary heat sources located at distances $\pm 2jD$ above and below the upper surface of the plate as shown in Fig. 4. The overall temperature in the plate is obtained by using equation (6) to determine the contribution of each individual heat source and then adding the contributions from all of these imaginary sources. Thus, equation (6) takes the form of a convergent series as follows

$$T - T_0 = \frac{Q_w}{\pi \rho C_p} \sum_{j=-\infty}^{\infty} \int_0^\infty \frac{1}{(4\pi \alpha t)^{1/2} (2\alpha t + \sigma^2)} \exp \left\{ \frac{-[(x+vt)^2 + y^2]}{(4\alpha t + 2\sigma^2)} - \frac{(z+2jD)^2}{4\alpha t} \right\} dt \quad (7)$$



5 Definition of the DSAW process for the analytical model

Again, it can be shown that equation (8) reduces to Rosenthal’s^{21,22} finite thickness plate solution for welding with a point source, i.e.

$$T - T_0 = \sum_{j=-\infty}^{\infty} \frac{Q_w}{2\pi k_t r_D} \exp \left[\frac{-v(x+r_D)}{2\alpha} \right] \quad (8)$$

where $r_D = [x^2 + y^2 + (2jD+z)^2]^{1/2}$ by allowing σ to go to zero and t to go to a very long time, i.e. $t \rightarrow \infty$.

As previously mentioned, the DSAW process has two separate heat sources, one acting on the top surface and one on the bottom surface of the plate. Therefore, the temperature at any point within the plate will be given by the temperature increase due to the PAW arc acting on the top surface of the plate and the temperature rise due to the GTAW arc acting on the bottom surface of the plate as shown in Fig 5. In this case, the net heat introduced by the PAW torch is given by

$$Q_P = \eta_{PP} E_{PP} I \quad (9)$$

where η_{PP} is the arc efficiency of the VPPAW process, E_{PP} is the arc voltage between the PAW torch and the plate and I is the total welding current. Similarly, the net heat introduced by the GTAW torch is

$$Q_G = \eta_{GP} E_{GP} I \quad (10)$$

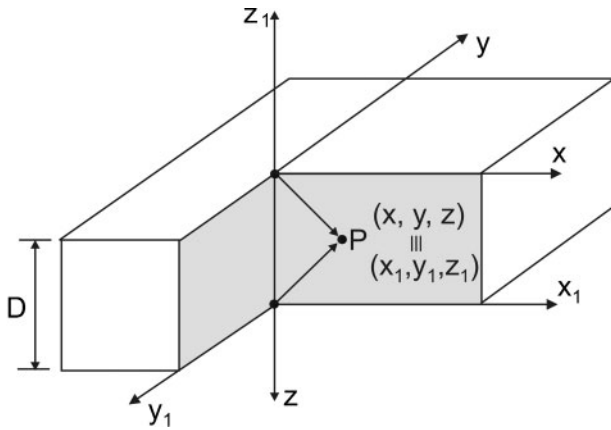
where η_{GP} is the arc efficiency of the GTAW process and E_{GP} is the arc voltage between the GTAW torch and the plate. Note that it is assumed that there is negligible potential drop across the AA5182 Al sheet due to the low resistivity of the alloy ($\rho = 55 \cdot 6 \text{ n}\Omega \text{ m}^{-1}$).³⁶ Thus, the net heat introduced into the plate by both sources is

$$Q_W = \eta EI = Q_P + Q_G = \eta_{PP} E_{PP} I + \eta_{GP} E_{GP} I \quad (11)$$

and from equation (11), the total arc efficiency of the DSAW process is given by

$$\eta = \eta_{PP} \left(\frac{E_{PP}}{E} \right) + \eta_{GP} \left(\frac{E_{GP}}{E} \right) \quad (12)$$

In order to combine the temperature distributions created by the separate PAW and GTAW arcs, one coordinate system will be transformed into the other coordinate system and the principle of superposition as described and used by Grong³⁴ will be applied. For this study, the coordinate system for the top PAW arc will remain the same while the coordinate system for GTAW arc will be changed by inverting the z axis as illustrated in Fig. 6. Thus, in order to convert the coordinate



6 Schematic representation of the DSAW heat source model with two coordinate systems: one for the PAW torch on top (x, y, z), and one for the GTAW torch below (x_1, y_1, z_1)

system for the GTAW torch into that for the PAW torch, the following transformations are used

$$x_1 = x, y_1 = -y \text{ and } z_1 = D - z \quad (13)$$

Considering the influence of only the PAW arc on the change in temperatures within the plate at a given point (x, y, z) in the plate and using equation (7), the change in temperature T_P , due to the PAW arc is given by

$$T_P = \frac{Q_p}{\pi \rho C_p} \sum_{j=-\infty}^{\infty} \int_0^{\infty} \frac{1}{(4\pi \alpha t)^{1/2} (2\alpha t + \sigma_p^2)} \exp \left\{ -\frac{[(x+vt)^2 + y^2]}{(4\alpha t + 2\sigma_p^2)} - \frac{(z+2jD)^2}{4\alpha t} \right\} dt \quad (14)$$

where σ_p is the distribution coefficient of the PAW arc. Similarly, the influence of only the GTAW arc on the change in temperatures within the plate at a given point (x_1, y_1, z_1)= $[x, -y, (D-z)]$ in the plate is obtained again using equation (7), i.e.

$$T_G = \frac{Q_G}{\pi \rho C_p} \sum_{j=-\infty}^{\infty} \int_0^{\infty} \frac{1}{(4\pi \alpha t)^{1/2} (2\alpha t + \sigma_G^2)} \exp \left\{ -\frac{[(x+vt)^2 + y^2]}{(4\alpha t + 2\sigma_G^2)} - \frac{[(D-z)+2jD]^2}{4\alpha t} \right\} dt \quad (15)$$

where σ_G is the distribution coefficient of the GTAW arc. Finally, the two distributions can be combined using the principle of superposition to obtain the temperature within the DSAW welded plate, i.e.

$$T(x, y, z) - T_0 = T_P(x, y, z) + T_G(x_1, y_1, z_1) \quad (16)$$

Double sided arc welding model implementation and validation

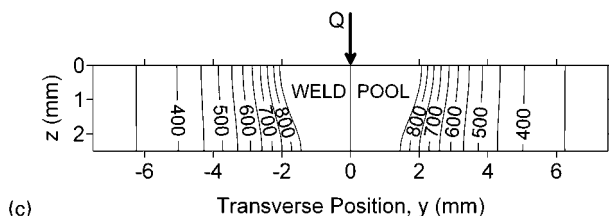
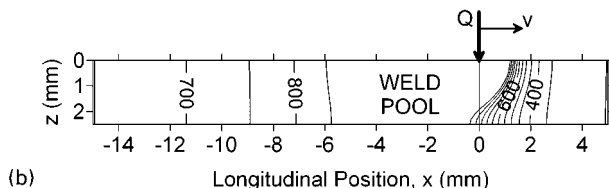
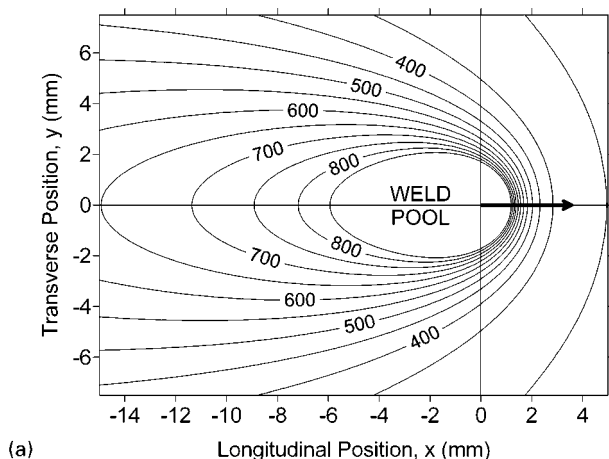
The analytical integral solution for temperature in conduction mode DSAW (equations (14)–(16)), was implemented and solved using Mathcad 14.0 software.³⁸ To test the derivation and implementation of the model,

the model was compared to the Rosenthal's 3D and finite plate thickness point heat source analytical thermal models (equations (5) and (8)) respectively.^{21,22} It was also compared to the predictions from Cline and Anthony's³² and to Eagar and Tsai's³³ 3D Gaussian distributed heat source analytical thermal mode (equation (6)). For these simulations, the bottom GTAW arc in the DSAW model was effectively turned off by setting $\eta_{GP}=0$ and a plate of infinite thickness was modelled by specifying a very large value for the plate thickness. The point heat source was modelled approximately using a very small Gaussian distribution coefficient, i.e. σ_{PP} was set to a value of 0.001 mm. The thermophysical material properties shown in Table 1 were used and the net welding power was maintained at 1500 W. Finally, when solving equations (14) and (15), it was not necessary to sum all solutions for $j=-\infty$ to ∞ , rather, by noting that the contribution to the change in temperature of each successive image of the heat source j , decreases exponentially as the absolute value of j increases, the summation was performed and j incremented only until the largest contribution to change in temperature for an image j , was below a desired threshold, e.g. 0.001 K. Typically, for thick plates, only a single solution for $j=0$ was required whereas thin plates required more images to satisfy the desire temperature threshold (typically <20).

In all cases, there was excellent agreement between the temperatures predicted by the DSAW model, Rosenthal's^{21,22} solutions, and Cline and Anthony's³² and Eagar and Tsai's³³ solutions. The results of representative simulations of single sided PAW or GTAW welds made in 2.5 mm thick AA5182 sheet at 50 mm s⁻¹ using 1500 W welding power are shown in Figs. 7 and 8. In Fig. 7, a point heat source, finite thickness plate model was used, i.e. Rosenthal's finite plate thickness model (equation (8)).^{21,22} Predictions by the DSAW model with $\sigma=0.001$ mm and $\eta_{GP}=0$ were identical. In Fig. 8, a more realistic Gaussian distributed heat source with $\sigma=2.0$ mm was used in the DSAW model again with $\eta_{GP}=0$. This distribution coefficient is consistent with the experimental measurements of σ by Smartt *et al.*,²⁹ Tsai and Eagar³⁰ and Lu and Kou³¹ when using this welding arc power and arc gap.

In Fig. 7a, the predicted weld pool profile on the top surface of the plate exhibits the classic elongated tear drop shape with a weld width of 4.16 mm. As shown in Fig. 7b and c, the weld is predicted to be full penetration. Note also that the isotherms are perpendicular to the top and bottom surfaces of the sheet as required for the specified adiabatic boundary conditions.

As may be seen through comparison of Figs. 7 and 8, there are significant differences in the predicted weld pool shape and size when the heat source is changed from a point heat source (Fig. 7) to a more realistic Gaussian distributed heat source (Fig. 8). In the latter case, the weld pool is less elongated and wider. The total weld pool width was predicted to be 4.75 mm. The most notable difference is that the weld is now only partial penetration with a weld pool depth less than half the sheet thickness (see Fig. 8b and c). As well, the maximum depth of penetration does not occur directly under the welding arc, rather, the weld pool depth increases steadily from the front of the weld pool over a longitudinal distance of ~4 mm to reach a maximum



a top surface isotherms; b longitudinal centreline isotherms; c transverse isotherms at $x = -1.88$ mm

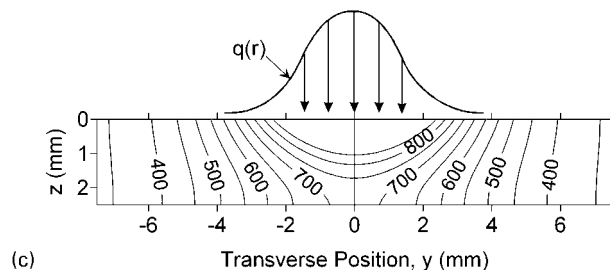
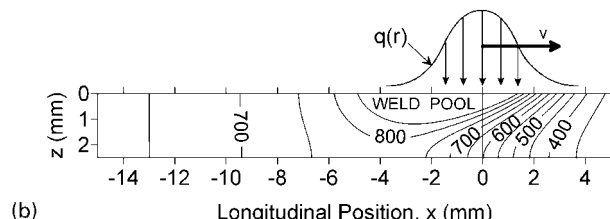
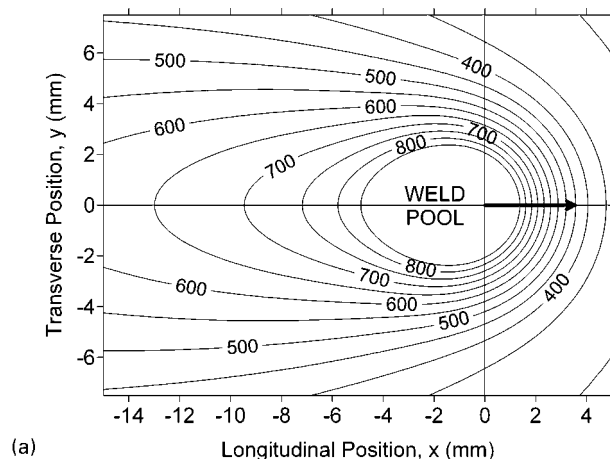
7 Isothermal profiles in 2.5 mm thick AA5182 sheet predicted by DSAW model and Rosenthal's point source, finite thickness plate model (equation (8)), using $Q=1500$ W and $v=50$ mm s^{-1}

value which occurs at a distance of ~ 2.5 mm behind the centre of the Gaussian distributed welding arc where the arc heat flux is now reduced to only a small fraction of the peak heat flux. These simulations clearly demonstrate the significant effects of the nature and distribution of the arc heat source used on the predicted weld pool shape and dimensions in the AA5182 sheets.

Double sided arc welding model calibration

In order to predict the DSAW weld dimensions and temperatures within the plate with the DSAW model (equations (14)–(16)), values of the arc efficiency and distribution coefficients of the PAW and the GTAW arcs must be determined. Arc efficiency values for the AC GTAW process have been reported to be between 20 and 50%,^{30,31,39} while arc efficiency values for AC PAW have been reported to be between 48 and 66%.^{40,41} The arc heat flux distribution coefficients for GTAW arcs have been reported to be between 1.6 and 2.5 mm depending on the welding current and arc gap.^{29–31} Even though it is known that the arc heat flux distribution for the PAW arc is constrained by the nozzle orifice size, measured values have not been reported in the literature.

A series of DSAW experiments were performed in order to determine η_{PP} , η_{GP} , σ_P and σ_G for calibration of the DSAW model. For these experiments, a PAW torch



a top surface isotherms; b longitudinal centreline isotherms; c transverse isotherms at $x = -1.46$ mm

8 Isothermal profiles in 2.5 mm thick AA5182 sheet predicted by DSAW model using $Q=1500$ W, $\sigma=2.0$ mm on top surface only and $v=50$ mm s^{-1}

was used on the top and a GTAW torch on the bottom of the sheet. A Miller Aerowave AC/DC power supply was used and operated in the constant current, square wave AC mode at a frequency of 60 Hz. The PAW torch was connected via the plasma console to the positive terminal of the power supply and the GTA torch was connected to the negative terminal. The preset welding torch parameters used for the DSAW experiments are shown in Table 2. A detailed description of the DSAW experimental equipment and procedures used may be found in Refs. 19 and 20.

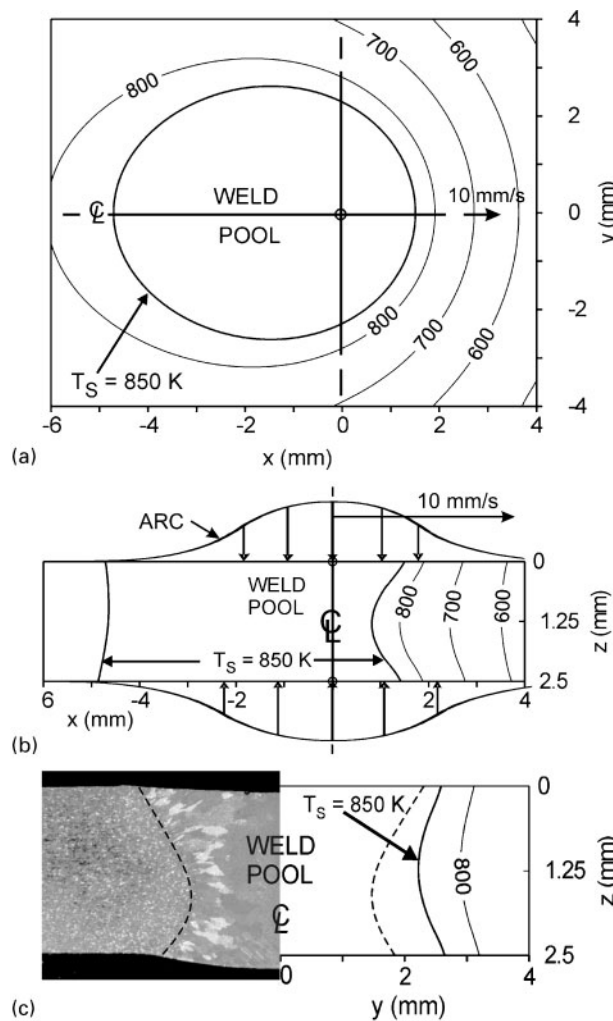
Table 2 Constant preset welding parameters used for top PAW torch and bottom GTAW torch

Torch parameter	PAW	GTAW
Arc gap, mm	6.25	5.0
Orifice diameter, mm	3.2	–
Plasma gas	UHP Ar	–
Plasma gas flow rate, L min^{-1}	0.45	–
Shielding gas	UHP Ar	Ar
Shielding gas flow rate, L min^{-1}	19	30
Electrode composition	W-1Zr	W-1Zr
Electrode diameter, mm	4.8	3.2
Electrode angle, °	20	60
Electrode truncation, mm	1.0	0.3

Double sided arc welding welds were made on 2.5 mm thick AA5182 alloy sheet using a nominal welding current of 60 A and welding speeds of 10, 14 and 18 mm s⁻¹. Since σ_P and σ_G strongly influence the weld widths, and η_{PP} and η_{GP} directly affect the total heat input and therefore cross-sectional area of weld metal, the DSAW weld widths were measured to help define σ_P and σ_G , and the depths of the separate top and bottom partial penetration welds produced at 18 mm s⁻¹ were measured in order to help define η_{PP} and η_{GP} . Values for σ_P and σ_G were obtained by adjusting σ_P and σ_G in the analytical model until there was good correlation between predicted and measured weld widths. Similarly, values of η_{PP} and η_{GP} were adjusted in the model until there was good correlation between predicted and measured weld areas of the separate top and bottom partial penetration welds produced at 18 mm s⁻¹. This required some iteration as there is a synergistic interaction between the effects of σ_P , σ_G , η_{PP} and η_{GP} on the predicted weld dimensions.

The preset and measured weld parameters and dimensions of the welds produced in the 2.5 mm thick sheet at 10, 14 and 18 mm s⁻¹ are shown in Table 3. Figures 9–11 show the predicted top surface, longitudinal centreline surface and transverse temperature profiles of the DSAW welds. The transverse profiles have been superimposed on photographs of the welds obtained at the three welding speeds. The values found to give the best correlation between predicted and observed DSAW weld dimensions were: $\eta_{PP}=0.35$, $\sigma_{PP}=1.8$ mm, $\eta_{GP}=0.49$ and $\sigma_{GP}=2.1$ mm. Thus, using equation (12), the value of the overall arc efficiency for the DSAW process was $\eta=0.42$. These values are within the range of previously reported values for these processes.^{30,31,40,41} As expected, the distribution coefficient of the constricted PAW arc was predicted to be less than the GTAW arc. Also, the arc efficiency of the PAW arc is significantly lower than the GTAW arc due to the additional heat lost to the water cooled orifice cup. Fuerschbach and Knorovsky⁴¹ have also observed lower arc efficiency values of the PAW process relative to the GTAW process and attributed this decreased efficiency to the heat transferred and lost to the constricting orifice cup in the PAW torch.

As may be seen in Figs. 9–11, as the welding speed increased, the weld pool became smaller and more elongated and changed from full penetration to an hour glass profile and finally to two separate partial penetration welds at the highest welding speed. Also, in the longitudinal profiles presented in Figs. 9b–11b, the centres of the Gaussian distributed welding arcs move forward towards the front of the weld pool as the



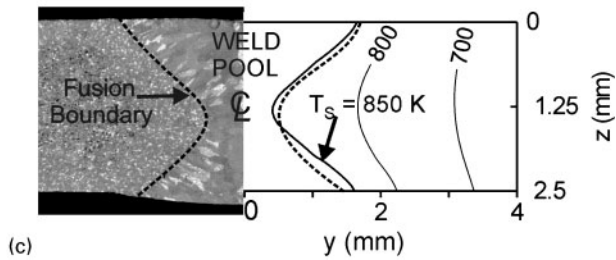
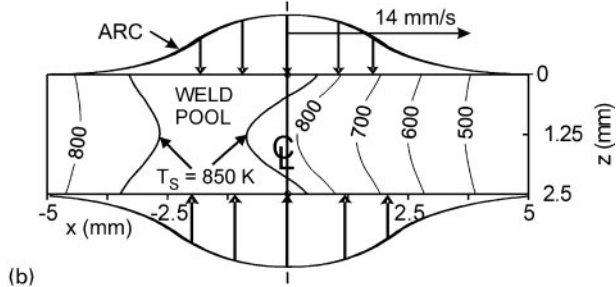
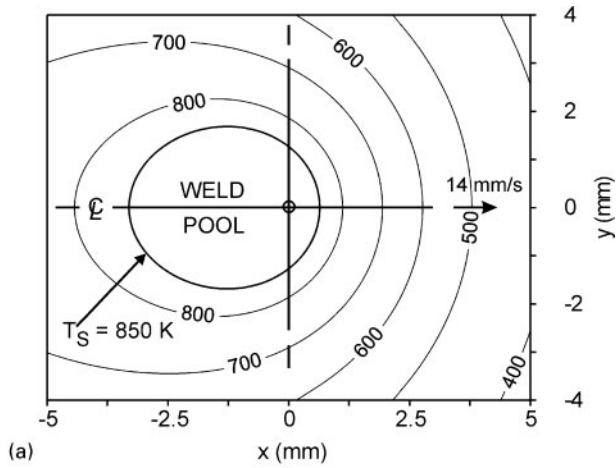
a top surface isotherms; b longitudinal centreline isotherms; c transverse isotherms at $x=-1.46$ mm with observed DSAW weld (left) and fusion boundary (broken line)

9 Predicted temperatures for full penetration DSAW weld made in 2.5 mm thick AA5182 sheet using total welding power of 1.67 kW and welding speed of 10 mm s⁻¹

welding speed increased. In fact, at the highest welding speed (18 mm s⁻¹, see Fig. 11b), melting is only predicted to begin at the centre of the arc, well behind the leading edge of the arc. Finally, there is excellent correlation between the predicted and observed weld pool shapes and sizes except at the slowest welding speed of 10 mm s⁻¹. The predicted weld pool of the 10 mm s⁻¹ weld was noticeably larger than the observed weld (see Fig. 9c). This is thought to be due to the

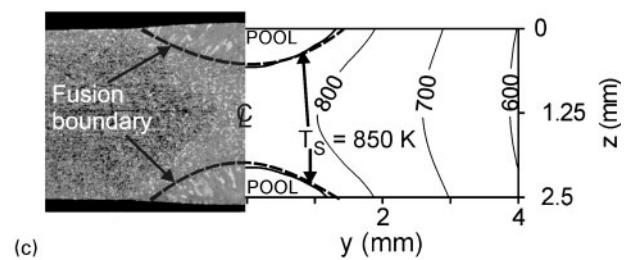
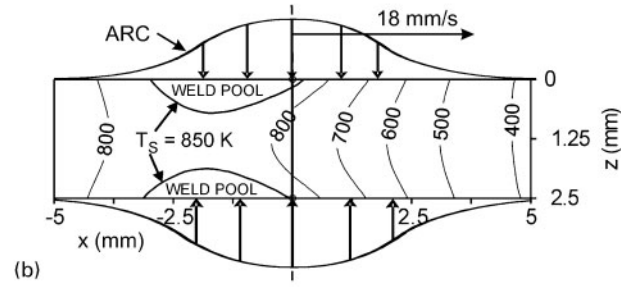
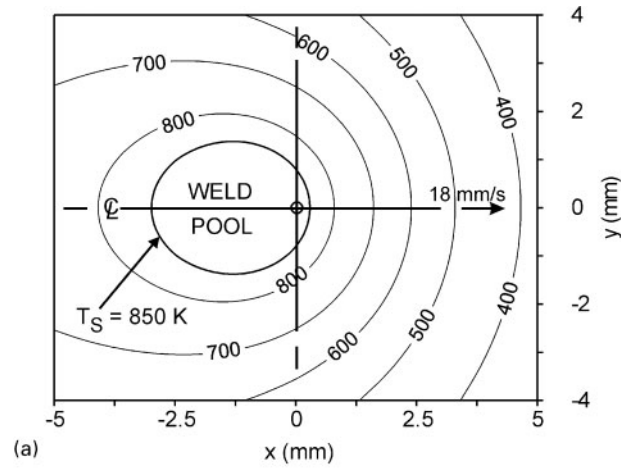
Table 3 Preset and measured weld parameters and dimensions of three DSAW welds made in 2.5 mm thick AA5182 Al alloy sheet at 10, 14 and 18 mm s⁻¹

Weld Parameter	Weld no. 1	Weld no. 2	Weld no. 3
Welding speed, mm s ⁻¹	10.0	14.0	18.0
Current, A	58.6	59.2	60.0
E_{PP} , V	15.3	15.4	16.6
E_{GP} , V	13.3	13.4	14.4
Total power, kW	1.67	1.70	1.86
Top weld width, mm	4.12 ± 0.1	3.45 ± 0.06	2.6 ± 0.1
Top weld depth, mm	Full penetration	Full penetration	0.53 ± 0.05
Bottom weld width, mm	3.9 ± 0.1	3.17 ± 0.05	2.56 ± 0.01
Bottom weld depth, mm	Full penetration	Full penetration	0.53 ± 0.01



a top surface isotherms; b longitudinal centreline isotherms; c transverse isotherms at $x = -1.25$ mm with observed DSAW weld (left) and fusion boundary (broken line)

10 Predicted temperatures for full penetration DSAW weld made in 2.5 mm thick A5182 sheet using total welding power of 1.70 kW and welding speed of 14 mm s^{-1}



a top surface isotherms; b longitudinal centreline isotherms; c transverse isotherms at $x = -1.4$ mm with observed DSAW weld (left) and fusion boundary (broken line)

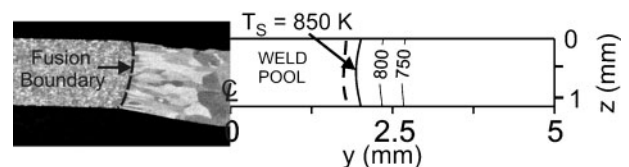
11 Predicted temperatures for partial penetration DSAW weld made in 2.5 mm thick A5182 sheet using total welding power of 1.86 kW and welding speed of 18 mm s^{-1}

additional heat lost by conduction through the sheet to the clamping bars which were only 10 mm from the weld centreline. This heat loss increases as the welding speed decreases and the width of the weld pool and isotherms increase and grow closer to the relatively cold clamping bars. This effect of the additional heat loss to nearby clamping fixtures on reduced weld pool size and overall welding process efficiency has been previously reported and described by others including, for example, Fuerschbach and Knorovsky⁴¹ in their study of arc efficiency of the GTAW and PAW processes and by Biglou *et al.*^{42,43} in their study of GTAW of plain carbon sheet steel.

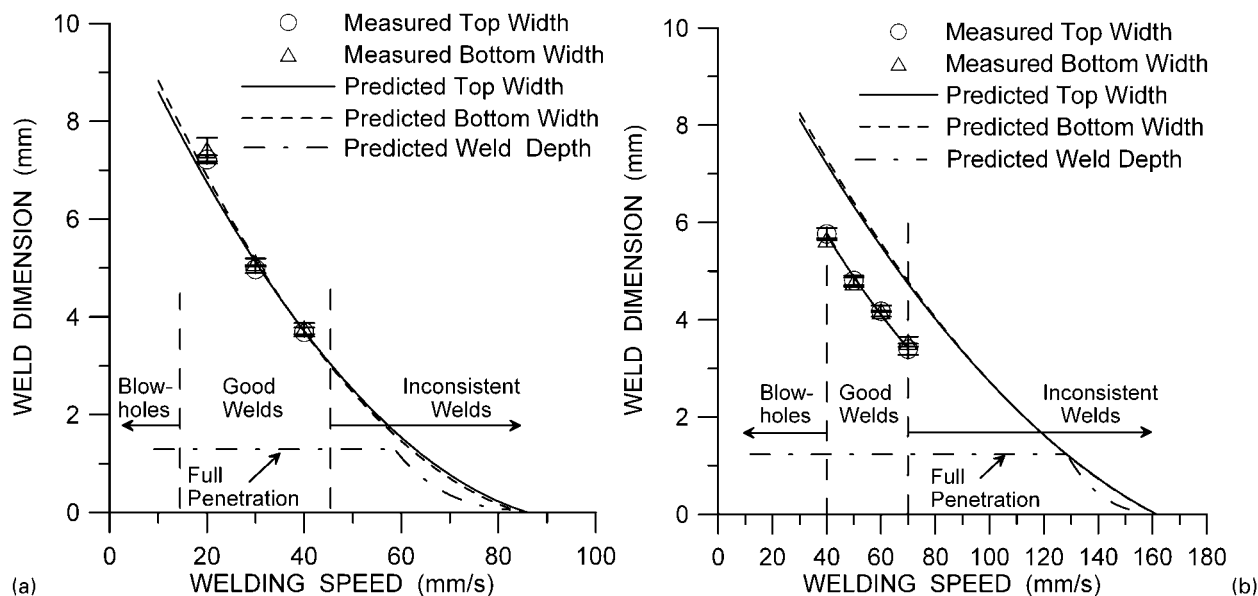
Predictions of DSAW weld geometry and temperatures

The values for arc efficiencies and arc distribution coefficients obtained in the previous section were used to predict the weld geometries of the DSAW welds made in the thinner 1.15 mm thick AA 5182 alloy sheets using

welding speeds from 20 to 80 mm s^{-1} and welding powers of 2.1 and 3.4 kW. For example, Figure 12 is a direct comparison between a transverse section through a weld produced in 1.15 mm thick sheet using a welding speed of 40 mm s^{-1} and welding power of 2.1 kW and the predicted isothermal profile. The broken lines are the observed fusion boundaries and the solid lines are the predicted isotherms. As may be seen, there is good



12 Comparison between DSAW weld made in 1.15 mm thick AA5182 sheet using welding speed of 40 mm s^{-1} and welding power of 2.1 kW and weld profile predicted using DSAW model: broken lines are fusion boundaries and solid lines are predicted isotherms



13 Measured and predicted DSAW weld dimensions in 1.15 mm thick AA5182 sheet versus welding speed using welding power of a 2.1 kW and b 3.4 kW (overall arc efficiency, $\eta=42\%$)

correlation between the measured and predicted weld widths.

Figure 13 shows plots of the predicted and measured weld dimensions versus welding speed. When using a welding power of 2.1 kW (see Fig. 13a), blowholes occurred on the DSAW welds made at welding speeds less than 14 mm s⁻¹.^{19,20} Blowhole defects were observed periodically along the DSAW weld beads when the energy input per unit length was too large, i.e. either the power input was excessive and arc forces were sufficient to blow a hole through the weld pool, or the welding speed was too slow and the weld width and weld pool were too large relative to the sheet thickness.^{19,20} Good welds were made using welding speeds between 20 and 40 mm s⁻¹, while no welds were produced at speeds above ~45 mm s⁻¹ as there was inconsistent cathodic cleaning of the oxide and arc coupling with the sheets above this speed. This caused a rapid decrease in weld quality and lack of fusion defects.^{19,20}

In Fig. 13a, there is very good agreement between the predicted and the observed top and bottom weld widths of the good welds made using 2.1 kW welding power. As the welding speed increased, the heat input per unit distance decreased resulting in a decrease of both the top and the bottom weld widths. All welds produced using 2.1 kW welding power were full penetration. This was correctly predicted by the model. Full penetration welds were predicted by the model for welding speeds up to 60 mm s⁻¹. Above this speed, only partial penetration welds are predicted with a rapid decrease in penetration. No melting of the sheets is predicted at speeds greater than 85 mm s⁻¹.

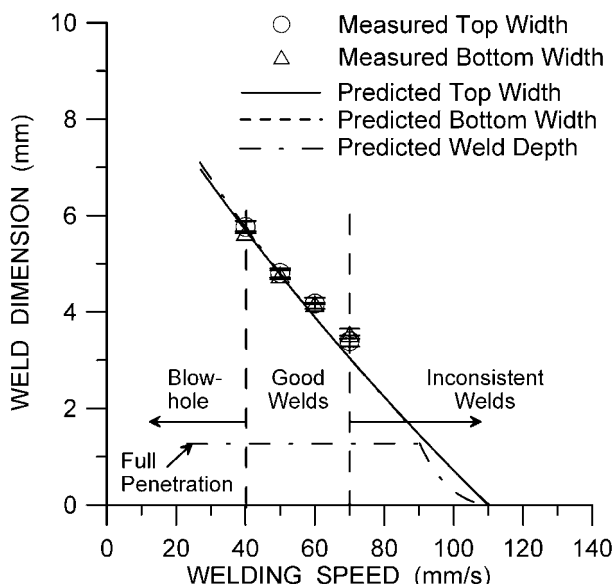
Figure 13b shows the observed and predicted weld dimensions versus welding speed for the welds produced using a higher weld power of 3.4 kW. At this power, blowholes were observed in the DSAW welds when the welding speed was less than 40 mm s⁻¹.^{19,20} Good welds were produced at welding speeds between 40 and 70 mm s⁻¹. Finally, no welds were produced at welding speeds greater than 70 mm s⁻¹ due to inconsistent cathodic cleaning of the oxide and arc coupling with the sheets.

The trends exhibited in Fig. 13b are similar to those observed at the low welding power, i.e. with increasing welding speed, the heat input per unit distance decreased and this resulted in a decrease of both the top and the bottom weld widths. At this higher welding power, however, the welds are predicted to be full penetration at welding speeds up to 130 mm s⁻¹. Above this speed, only partial penetration welds with rapidly decreasing penetration are predicted. No melting of the sheets is predicted at speeds greater than 160 mm s⁻¹.

In Fig. 13b, significant discrepancies between the predicted and measured weld widths are evident. Notably, the weld dimensions are consistently over predicted by between 21 and 46%. Smartt *et al.*²⁹ reported that arc efficiencies in the GTAW process decrease as the welding current and voltage (i.e. welding power) are increased. Ghent *et al.*⁴⁴ also reported that arc efficiencies in stationary GTAW welds decreased 23% (from 74 to 57%) when the total DCEN input power was increased from 1.8 to 3.4 kW. This suggests that better agreement between the predicted and measured DSAW weld widths would be obtained by decreasing the arc efficiencies of both the PAW and GTAW arcs. As shown in Fig. 14, there is now much better correlation between the predicted and observed weld dimensions when the overall arc efficiency was decreased from 42 to 34%. The differences between the predicted and observed good weld dimensions are now between 0 and 3%. Partial penetration welds are now predicted to occur when the welding speed exceeds 90 mm s⁻¹ and no melting is predicted above 110 mm s⁻¹.

Conclusions

An analytical thermal model of the DSAW process has been developed that includes two Gaussian distributed arcs: one from the PAW torch acting on the top surface of 1.15 and 2.5 mm thick AA5182 Al alloy sheets and the other from the GTAW torch acting on the bottom surface of the sheets. Predictions from this model clearly show the beneficial effects of using a more realistic Gaussian distributed heat sources and finite plate



14 Measured and predicted DSAW weld dimension in 1.15 mm thick AA5182 sheet versus welding speed using welding power of 3.4 kW and overall arc efficiency η of 36%

thickness solution on the accuracy of the predictions of the absolute size and shape of conduction mode DSAW welds made in these Al alloy sheets. The model has been shown to be capable of resolving and correctly predicting the synergistic effects of the arc efficiency and arc distribution coefficient of both arcs on the DSAW weld pool dimensions and shape. Thus, provided appropriate values for arc efficiencies and distribution coefficients are used, the DSAW model is capable of accurately predicting the weld dimensions of both full and partial penetration conduction mode DSAW welds in Al alloy sheets as a function of the welding process parameters such as welding speed and welding power. Moreover, this model is capable of predicting the weld pool shape and size of DSAW welds over a wide range of process conditions from those that produce 2D full penetration welds at slow speeds to severe hour glass shaped full penetration welds at intermediate welding speeds to separate partial penetration weld pools on the top and bottom of the sheet at high welding speeds. In addition, the model can be used to predict the welding speed at which there is a transition from full to partial penetration as well as the speed above which no melting occurs, thus making it a valuable tool for weld procedure development.

When using a square wave AC power supply and a total power of 1.8 kW, the overall arc efficiency of the DSAW process was found to be 42% and the heat distribution coefficients for the PAW arc and the GTAW arc were 1.8 and 2.1 mm respectively. The arc efficiencies of the GTAW and PAW torches were found to be 49 and 35% respectively. The lower PAW arc efficiency was attributed to heat lost to the water cooled orifice cup in the PAW torch. The overall DSAW arc efficiency was found to decrease from 42 to 34% as the total welding power increased from 1.8 to 3.4 kW.

Acknowledgements

This work was supported by the Natural Sciences and Engineering Research Council of Canada. The authors

wish to thank also Alcan International Research Labs, Kingston, ON, Canada for supplying the AA 5182 project alloy sheet used in the experimental validation experiments.

References

1. E. Kubel: *Manuf. Eng.*, 1997, **119**, (5), 38–45.
2. R. J. Kazmier: *Adv. Mater. Process.*, 2001, **94**, (1), 42–44.
3. S. Das: *Adv. Mater. Process.*, 2000, **157**, (3), 41–42.
4. E. Craig: *Weld. J.*, 1998, **67**, (2), 19–25.
5. J. C. Ion: *Sci. Technol. Weld. Join.*, 2000, **5**, (5), 265–276.
6. H. Zhao, D. R. White and T. DebRoy: *Int. Mater. Rev.*, 1999, **44**, (6), 238–266.
7. M. Pastor, H. Zhao, R. P. Martukanitz and T. DebRoy: *Weld. J.*, 1999, **78**, (6), 207s–216s.
8. M. G. Deutsch, A. Punkari, D. C. Weckman and H. W. Kerr: *Sci. Technol. Weld. Join.*, 2003, **8**, (4), 246–256.
9. A. Punkari, D. C. Weckman and H. W. Kerr: *Sci. Technol. Weld. Join.*, 2003, **8**, (4), 269–282.
10. M. Deutsch: 'Effects of Nd:YAG laser welding and VPPAW welding process variables on weld metal geometry and defects of 1.6 mm thick 5182 aluminum', MSc thesis, University of Waterloo, Canada, 2002.
11. A. Punkari: 'Variable polarity plasma arc welding and dual-beam Nd:YAG laser welding of aluminum alloys', MSc thesis, University of Waterloo, Canada, 2002.
12. Y. M. Zhang and S. B. Zhang: 'Method of arc welding using dual serial opposed torches', US patent no. 5 990 446, 23 November 1999.
13. Y. M. Zhang and S. B. Zhang: *Weld. J.*, 1998, **77**, (6), 57–61.
14. Y. M. Zhang and S. B. Zhang: *Weld. J.*, 1999, **78**, (6) 202s–206s.
15. Y. M. Zhang, C. Pan and A. T. Male: *J. Mater. Sci. Lett.*, 2000, **19**, 831–833.
16. Y. M. Zhang, C. Pan and A. T. Male: *Metall. Mater. Trans. A*, 2000, **31A**, 2537–2543.
17. Y. M. Zhang, C. Pan and A. T. Male: *Mater. Sci. Technol.*, 2001, **17**, (10), 1280–1284.
18. Y. M. Zhang, S. B. Zhang and M. Jiang: *Weld. J.*, 2002, **81**, (11), 249s–255s.
19. Y. Kwon: 'Double-sided arc welding of AA5182 aluminum alloy sheet', MSc thesis, University of Waterloo, Canada, 2003.
20. Y. Kwon and D. C. Weckman: *Sci. Technol. Weld. Join.*, 2008, **13**, (6), 485–495.
21. D. Rosenthal: *Trans. ASME*, 1946, **43**, (11), 849–866.
22. D. Rosenthal: *Weld. J.*, 1941, **20**, 220s–234s.
23. D. T. Swift-Hoof and A. E. F. Gick: *Weld. J.* 1973, **52**, (11), 492s–499s.
24. D. Honggang, G. Hongming and W. Lin: *Int. J. Numer. Methods Eng.*, 2006, **65**, 1673–1687.
25. F. M. Zhou, Y. S. Yu, Y. H. Feng, Y. C. Huang and Y. Y. Qian: *Sci. Technol. Weld. Join.*, 2003, **8**, (1) 76–8.
26. C. S. Wu and J. S. Sun: *Comput. Mater. Sci.*, 2002, **25**, (3), 457–468.
27. K. Hong, D. C. Weckman and A. B. Strong: *Can. Metall. Q.*, 1998, **37**, (3–4), 293–303.
28. H. S. Carslaw and J. C. Jaeger: 'Conduction of heat in solids', 2nd edn; 1959, Oxford, Oxford University Press.
29. H. B. Smartt, J. A. Stewart and C. J. Einerson: Proc. '85 ASM Int. Welding Cong., ASM's Materials week '85, Toronto, Canada, October 1985, ASM Int., Paper 8511–011.
30. N. S. Tsai and T. W. Eagar: *Metall. Trans. B*, 1985, **16B**, 841–846.
31. M. Lu and S. Kou: *Weld. J.*, 1988, **67**(2), 29s–34s.
32. H. E. Cline and T. R. Anthony, *J. Appl. Phys.*, 1977, **48**, (9), 3895–3900.
33. T. W. Eagar and N. S. Tsai: *Weld. J.*, 1983, **62**, (12), 346s–355s.
34. Ø. Grong: 'Metallurgical modelling of welding', 2nd edn; 1997, London, The Institute of Materials.
35. O. Manca, B. Morrone and V. Naso: *Int. J. Heat Mass Transf.*, 1995, **38**, (7), 1305–1315.
36. in 'ASM Handbook', Vol. 2, 'Properties and selection: nonferrous alloys and special purpose materials', 10th edn, 95; 1990, Materials Park, OH, ASM International.
37. H. S. Carslaw and J. C. Jaeger: 'Conduction of heat in solids', 255; 1967, London, Oxford University Press.
38. Mathcad 14.0©, 2007, Parametric Technology Corp., Needham, MA, USA.
39. S. Kou: 'Welding metallurgy'; 1987, Toronto, John Wiley & Sons.

40. D. M. Evans, D. Huang, J. C McClure and A. C. Nunes: *Weld. J.*, 1988, **77**, (2), 53s–58s.
41. P. W. Fuerschbach and G. A. Knorovsky: *Weld. J.*, 1991, **70**, (11), 287s–297s.
42. J. Biglou, D. C. Weckman, G. W. Bennett and H. W. Kerr: *Sci. Technol. Weld. Join.*, 2001, **6**, (1), 51–62.
43. J. Biglou: 'GTA weld process modelling using principal component analysis techniques', MSc thesis, University of Waterloo, Canada, 1993.
44. H. W. Ghent, D. W. Roberts, C. E. Hermance, H. W. Kerr and A. B. Strong: Proc. Int. Conf. on 'Arc physics and weld pool behaviour', London, UK, May 1979, The Welding Institute, 17–23.